REGULARIZATION IN SLOPE TOMOGRAPHY

J. C. Costa, F. J. C. da Silva, E. N. S. Gomes, J. Schleicher, A. Mello, and D. Amazonas

email: *js@ime.unicamp.br*
keywords: *Stereotomography, model building, regularization*

ABSTRACT

Seismic imaging in depth is limited by the accuracy of velocity model estimation. Slope tomography uses the slowness components and traveltimes of picked reflection or diffraction events for velocity model building. The unavoidable data incompleteness requires additional information to assure stability to inversion. One natural constraint for ray based tomography is a smooth velocity model. We propose a new, reflection-angle-based kind of smoothness constraint as regularization in slope tomography and compare its effects to three other, more conventional constraints. The effect of these constraints are evaluated through angle domain common image gathers, computed with wave-equation migration using the estimated velocity model. We find the smoothness constraints to have a distinct effect on the velocity model but a weaker effect on the migrated data. In numerical tests on synthetic data, the new constraint leads to geologically more consistent models.

INTRODUCTION

The determination of a macrovelocity model is essential for time and depth imaging of seismic reflectors in the earth. Among the many methods that try to to achieve this aim are so-called tomographic methods that are based on the inversion of traveltimes of seismic reflection events. One of these is slope tomography, which uses slowness vector components to improve and stabilize the traveltime inversion. Slope tomography was initially proposed by Billette and Lambaré (1998) as a robust tomographic method for estimating velocity macro models from seismic reflection data. They had recognized the potential efficiency of traveltime tomography (Bishop et al., 1985; Farra and Madariaga, 1988) but also the difficulties associated with a highly interpretative picking. The selected events have to be tracked over a large extent of the pre-stack data cube, which is quite difficult for noisy or complex data. The idea is to use locally coherent events characterized by their slopes in the pre-stack data volume. Such events can be interpreted as pairs of ray segments and provide independent information about the velocity model.

However, the data for slope tomography are incomplete (Bishop et al., 1985). Therefore, stability and convergence can only be achieved if additional information is prescribed. These additional information contains desirable properties for the solution, reducing ambiguity (Menke, 1989). For ray based inversion, smoothness is a requirement, because rough models cause the forward problem to break down during linear iterations. The use of combined smoothness constraints enables an interpretation-oriented inversion while keeping solutions consistent with the data.

We investigate the effect of different kinds of smoothness constraints in slope tomography. The Marmousoft data set (Billette et al., 2003) is used for this study. Lateral, vertical and isotropic smoothing constraints are prescribed in different combinations. Moreover, we propose a structurally motivated smoothing constraint in the direction of a potential reflector. Angle domain common imaging gathers (ADCIG) are used to evaluate the quality of the estimated velocity models.

Here, we use a finite-difference implementation, but the correction can also be incorporated into Fourier-domain implentations like the one of Tessmer (2003).

METHOD

Slope tomography differs from conventional reflection tomography by the data that are used for the inversion (Billette et al., 2003). Firstly, the traveltimes are picked from locally coherent events that are interpreted as primary reflections or diffractions. Secondly, in-line slowness-vector components of these events, detected in common-shot or common-receiver gathers, are used in addition to source and receiver positions and traveltimes. Thus, the data space is given by

$$\mathbf{d} = [(\mathbf{x}^s, \mathbf{x}^r, s^s, s^r, T^{sr})_n] \qquad (n = 1, \ldots, N) \,, \tag{1}$$

where $\mathbf{x}^s$ and $\mathbf{x}^r$ are the source and receiver positions, T^{sr} are the traveltimes, and s^s and s^r are the slowness-vector projections into the receiver line. Moreover, N is the number of selected events.

Slope tomography also uses a different model parameterization than conventional reflection tomography. In 2D, the model to be estimated includes: the parameters describing the velocity model, $\mathbf{p}$, the scattering-point coordinates, $\mathbf{X}$, the emergence angles, θ^s and θ^r, and the ray traveltimes, τ^s e τ^r. In other words, the model vector is

$$\mathbf{m} = \{\mathbf{p}, (\mathbf{X}, \theta^s, \theta^r, \tau^s, \tau^r)_n\} \qquad (n = 1, \ldots, N) \,. \tag{2}$$

To solve the inverse problem using linear iterations, an initial reference model must be given. In this model $\mathbf{m}_0$, ray tracing is performed to calculate the synthetic data corresponding to equation (1), denoted as $\mathbf{d}^c$. The difference between the observed and calculated data, $\mathbf{d}^o - \mathbf{d}^c$, defines the deviation $\delta\mathbf{d}$.

This deviation is modeled in linear approximation as

$$\delta\mathbf{d} = \mathcal{D}\mathbf{F}(\mathbf{m}_0)\delta\mathbf{m} \,, \tag{3}$$

where $\mathcal{D}\mathbf{F}$ denotes the approximate operator describing the direct problem under variation of the reference model $\mathbf{m}_0$. The operator $\mathcal{D}\mathbf{F}(\mathbf{m}_0)$ is known as the Fréchet derivative (see, e.g., Menke, 1989). The solution of the linear system in equation (3) determines a new reference model

$$\mathbf{m}_0^{new} = \mathbf{m}_0 + \delta\mathbf{m}. \tag{4}$$

The process continues iteratively until the norm of the deviation $\|\delta\mathbf{d}\|$ is smaller than a given tolerance value (in case of convergence) or until a maximum number of steps. In this work, we use the standard L_2 norm (Menke, 1989).

In our implementation, we construct a model for the square of the medium velocity, which is represented using the tensor product of third-order B-splines as

$$p(x_1, x_3) \quad = \quad \sum_{\alpha=1}^{N_1} \sum_{\beta=1}^{N_2} p^{\alpha\beta} B_\alpha(x_1) B_\beta(x_3) \,, \tag{5}$$

where the functions $B_\gamma(x_j)$ are the base functions of the interpolator along x_j. Moreover, N_j indicates the number of B-spline nodes in that direction and $p^{\alpha\beta}$ are the interpolation coefficients. In other words, the coefficients $p^{\alpha\beta}$ constitute the actual medium parameters that are to be estimated by slope tomography.

Regularization

Due to the incompleteness of the data, additional conditions that take desirable properties of the solution into account, must be incorporated into the objective function. One necessary condition requires all model-parameter perturbations, computed in each linear iteration, to be small; other conditions are smoothness constraints on the velocity model.

Weak constraints are used to enforce smoothness of the solution. These constraints are applied in a least-squares sense at each node of the B-splines mesh, as indicate below. Several kinds of smoothness exist, one for lateral homogeneity, one for vertical homogeneity, one for minimum curvature along each Cartesian coordinate, and finally the minimum Laplacian, which minimizes the curvature of the velocity model isotropically. The specification of these constraints requires the evaluation of first and second partial
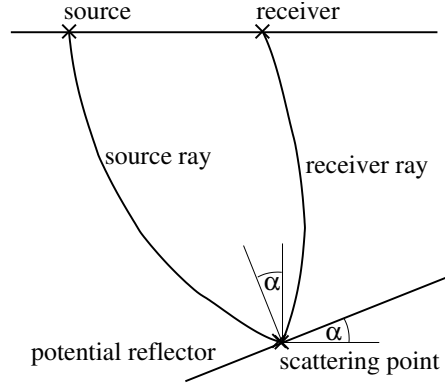
Figure 1: Position of a potential reflector.

derivatives of the velocity model with respect to the spatial coordinates. Denoting the spatial derivatives in the x_1 and x_3 directions by $\mathbf{D}_1$ and $\mathbf{D}_3$, these derivatives are computed in the form

$$
D_1^n p(x_1, x_3) \quad = \quad \sum_{\alpha=1}^{N_1} \sum_{\beta=1}^{N_2} p^{\alpha\beta} \frac{\partial^n B_\alpha(x_1)}{\partial x_1^n} B_\beta(x_3) \, , \tag{6}
$$

and correspondingly for the derivatives with respect to coordinate x_3.

Standard regularization of the derivatives along the coordinate directions can be improved by smoothing along the reflectors. Sinoquet (1993) proposed to use a priori geological information for this purpose in reflection tomography. In the same spirit, Clapp et al. (2004), who applied reflection tomography in order to better flatten post-tomography common-image gathers, pointed out the shortcomings of standard regularization strategies. To overcome these problems, they proposed to use a priori information about the reflector dip from previous migrations to design smoothing operators along the reflectors. By smoothing the velocity model along the reflectors, they were able to construct models that were more geologically reasonable, improved reflector positioning, and led to better focused images.

Actually, the distribution of the scattering points in depth provides a more natural way to enforce a geologically meaningful smoothing that does not rely on a priori information. Assuming that all events to be used in the tomographic inversion are reflections, the angle between the normal to the potential reflector and the vertical direction is (see Figure 1)

$$
\alpha = \frac{\theta_s + \theta_r}{2} \, , \tag{7}
$$

which is available at each iteration of slope tomography. Using this information, we tried to constrain the velocity model using the reflector geometry, requiring the model to be smooth along the tangent to the reflector at each scattering point. Computing the velocity gradient at the scattering point, $\mathbf{X}$, we add the regularization constraint

$$
\mathbf{n}(\alpha; \mathbf{X}) \times \nabla p(\mathbf{X}) = \mathbf{0} \, . \tag{8}
$$

This equation constrains the velocity gradient to be perpendicular to potential reflectors, thus smoothing the velocity model along them. We denote this smoothing operator by $\mathbf{D}_r$. In order to limit the increase in the size of the problem, we apply this constraint to a fraction of the scattering points. The proposed dip regularization is different from the approach of Clapp et al. (2004). In our approach, the dip information is not obtained from a previously migrated image, but from ray-tracing in the reference model during the inversion. Thus, the smoothing operator is updated at each iteration. The so-obtained dip information can be used for a futher refinement of the velocity model through residual moveout inversion of common image gathers.

Combining these regularizations, we use the objective function

$$
\begin{aligned}
\Phi(\mathbf{m}; \lambda_i) \quad = \quad & \|\mathbf{d} - \mathbf{F}(\mathbf{m})\|_2^2 + \lambda_0^2 \|\mathbf{m} - \mathbf{m}_0\|_2^2 \\
& + \lambda_1^2 \|\mathbf{D}_1^2 + \mathbf{D}_3^2 \mathbf{p}\|_2^2 + \lambda_2^2 \|\mathbf{D}_1^2 \mathbf{p}\|_2^2 + \lambda_3^2 \|\mathbf{D}_3^2 \mathbf{p}\|_2^2 \\
& + \lambda_4^2 \|\mathbf{D}_1 \mathbf{p}\|_2^2 + \lambda_5^2 \|\mathbf{D}_3 \mathbf{p}\|_2^2 + \lambda_6^2 \|\mathbf{D}_r \mathbf{p}\|_2^2 \,,
\end{aligned}
\tag{9}
$$

where the λ_i are Lagrangian multipliers that weight the contributions of regularization in the objective function. At each iteration we need to solve the linear system

$$
\begin{bmatrix}
\mathcal{D}\mathbf{F}(\mathbf{m}_0) \\
\lambda_0 \mathbf{I} \\
\lambda_1 (\mathbf{D}_1^2 + \mathbf{D}_3^2) \\
\lambda_2 \mathbf{D}_1^2 \\
\lambda_3 \mathbf{D}_3^2 \\
\lambda_4 \mathbf{D}_1 \\
\lambda_5 \mathbf{D}_3 \\
\lambda_6 \mathbf{D}_r
\end{bmatrix}
\delta\mathbf{m} =
\begin{bmatrix}
\delta\mathbf{d} \\
\mathbf{0} \\
\mathbf{0} \\
\mathbf{0} \\
\mathbf{0} \\
\mathbf{0} \\
\mathbf{0} \\
\mathbf{0}
\end{bmatrix} .
\tag{10}
$$

The prescription of λ_1, λ_2, λ_3, λ_4 and λ_5 determines the weight of isotropic curvature smoothing, lateral and vertical curvature smoothing, as well as lateral and vertical homogeneity, respectively. The value of λ_6 controls the degree of smoothing along potential reflectors.

This objective function gives us the flexibility to permit different assumptions about the velocity model. We test some of the possible choices and their effect on the estimated velocity models in the Numerical Examples section below.

Angle domain common imaging gathers

We use angle domain common imaging gathers (ADCIGs) to measure the quality of the velocity models estimated for seismic imaging. We compute ADCIGs using wide angle FFD migration with the complex Padé approximation (Amazonas et al., 2007). Based on the works of Rickett and Sava (2002), Sava and Fomel (2003), and Biondi (2006), we compute subsurface offset domain common image gathers (SOD-CIGs) using the imaging condition

$$
I(\xi, h) = \sum_\omega P_s^*(x - h, z; \omega) P_r(x + h, z; \omega) \,,
\tag{11}
$$

where P_s is the source wavefield at the imaging point ξ, P_r^* is the downward continued receivers wavefield at ξ, ω is the angular frequency, h is the subsurface offset and $(^*)$ denotes complex conjugate. The ADCIGs are then computed from the SODCIGs by the slant stack

$$
A(z, \tan\theta) = \int I(z + h\tan\theta, h)\, dh \,,
\tag{12}
$$

where θ is the scattering angle at the imaging point.

NUMERICAL EXAMPLES

Model

We use the Marmousoft data (Billette et al., 2003) to evaluate the effect of regularization constraints in slope tomography. These synthetic data are obtained by Born modeling in a smoothed version of the original Marmousi model (see Figure 2). The smoothing is done using a Gaussian filter minimizing with correlation-length $\tau = 240\ m$ (Billette et al., 2003). A correspondingly smoothed model is depicted in Figure 3. In these synthetic data, 5490 events were selected by an automated picking code (Billette et al., 2003). Their traveltimes and local slopes constitute the input data for the stereotomographic inversion in the numerical examples.
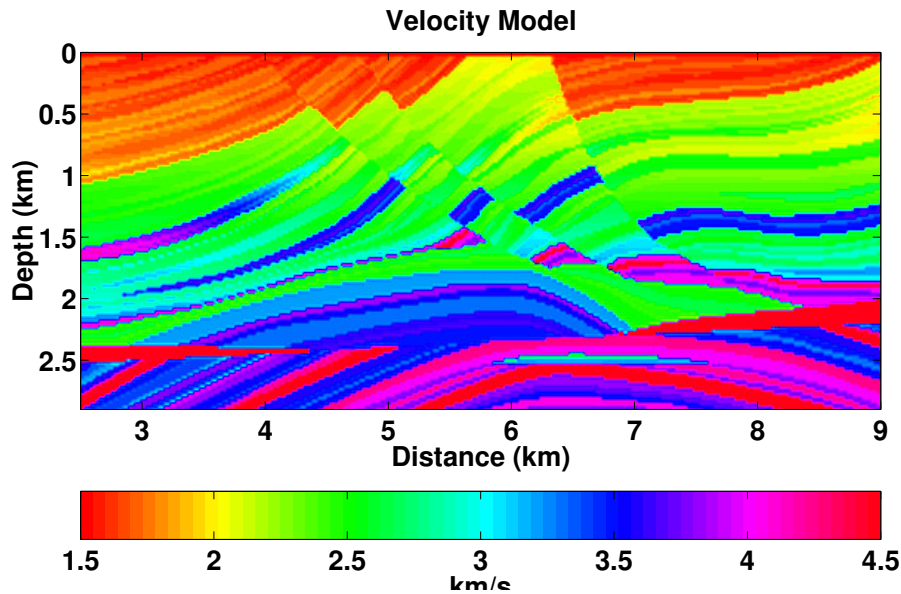
Velocity Model

Figure 2: Exact Marmousi velocity model.

Inversion results

Below, we discuss the results of slope tomography using five kinds of regularization strategies, being (1) isotropic smoothing of the curvature by minimizing the norm of the Laplacian of the velocity field; (2) anisotropic smoothing of the curvature by minimizing curvature independently in the lateral and vertical directions; (3) anisotropic smoothing of the heterogeneity by minimizing the velocity gradient independently in lateral and vertical directions; (4) structural smoothing of the heterogeneity by minimizing the velocity gradient along the reflectors; (5) anisotropic and structural smoothing of the heterogeneity by minimizing the velocity gradient both along the reflectors and laterally.

Our implementation of slope tomography uses the multigrid approach suggested by Billette et al. (2003). The inversion is performed initially on a sparse B-spline mesh, with 13×11 nodes. The nodes are spaced at 1 km laterally and 0.5 km vertically. The result of this inversion is the initial model for the final inversion on a dense B-spline mesh, with 61×51 nodes. Now, the nodes are spaced at 0.2 km laterally and 0.1 km vertically. The damping parameter, λ_0 is set to 0.025 for all inversions. We present the results after 30 linear iterations using the dense mesh.

In the first inversion, we only use the Laplacian operator, with $\lambda_1 = 0.005$. All other λ_i in equation (10) except for λ_0 are set to zero. The resulting estimated velocity model is shown in Figure 4. In the second inversion, the regularization minimizes the lateral and vertical curvatures independently, with $\lambda_1 = 0.050$ and $\lambda_2 = 0.010$. The estimated velocity model is shown in Figure 5. The third inversion minimizes heterogeneity, with $\lambda_4 = 0.050$ and $\lambda_5 = 0.010$. The resulting velocity model is depicted in Figure 6. The fourth inversion applies the proposed regularization, with $\lambda_6 = 0.050$. The estimated velocity model is shown in Figure 7. Our last inversion combines smoothing along the reflectors with a minimization of lateral inhomogeneity, with $\lambda_4 = 0.005$ and $\lambda_6 = 0.0025$. The estimated velocity model is shown in Figure 8.

The five estimated velocity models are quite different from the original smoothed Marmousi velocity model of Figure 3. We can see that the smoothness constraints have a distinctive effect on the estimated velocity models. The most obvious differences of the models occur in the bottom part where the data coverage is poorer. The curvature regularizations (Figures 4 and 5) tend to concentrate the high-velocity zone in the center of the model. The model in Figure 5 has more lateral smoothness than all the others. The inversions using gradient constraints (Figures 6, 7, and 8) distribute the high velocity over the whole model. They recover models that are more similar to the smoothed model of Figure 3 than the inversions using curvature restraints. The inversions that try to incorporate structural information (Figures 7 and 8) seem to best reconstruct some details of the smoothed model, like the higher velocity at $x = 7.2$ km and
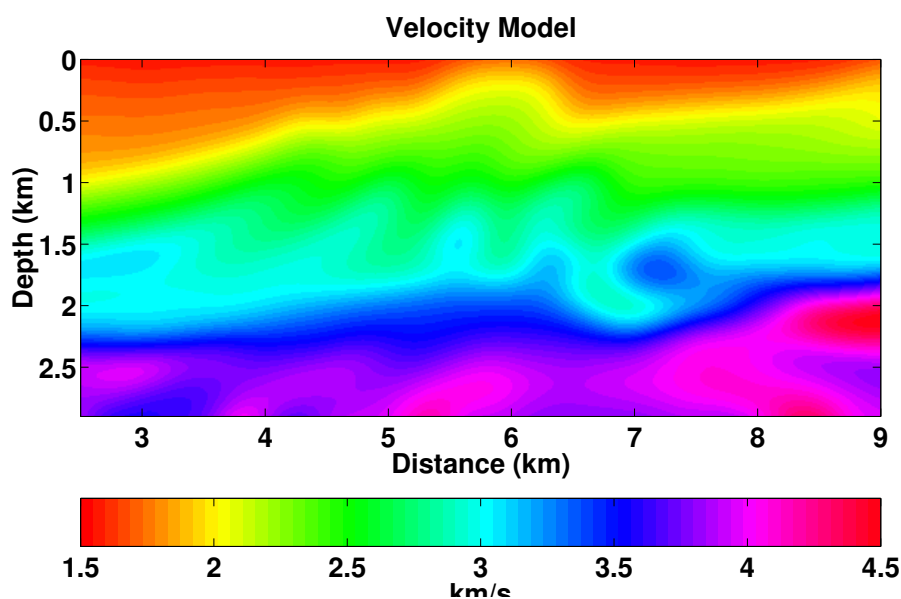
Figure 3: Smooth velocity model computed from the exact Marmousi model of Figure 2 by Gaussian smoothing.

$z = 1.6$ km, the lower velocity at $x = 6.8$ km and $z = 2.0$ km, or even the slightly increased velocity at $x = 2.6$ km and $z = 1.6$ km. Note that no inversion can be expected to recover the model below about $z = 2.2$ km, because the ray coverage is too poor.

Prestack migration

As the next step, we compare the migrated sections obtained from depth migrating the Marmousoft data using the velocity models estimated above. For comparison, we also show the migration result using the smoothed velocity model (see Figure 9). For the purpose of depth migration, we sampled the velocity models on a regular mesh with a grid spacing of 12.5 m. The resulting migrated images are depicted in Figures 10 through 14.

The high quality of the upper part of all migrated images confirms the quality of velocity model inversion by slope tomography. Where high ray coverage is achieved, the recovered model is very good. In these regions, the particular kind of regularization has not much influence on the inversion. On the other hand, in regions of low ray coverage, different regularizations lead to different models and, thus, to differences in the migrated images. The most dramatic difference between the images can be seen in the lower right corner. Clearly, the failure of the curvature constraints to yield high velocity in that region leads to a major pull-up of the reflectors (Figures 10 and 11). The migrated images obtained from the gradient constraints (Figures 12, 13 and 14) look much better. The left salt intrusion is almost perfectly positioned by all three of them. Even the right salt intrusion looks pretty similar to what it should be. Again, please note that at the borders of the model, ray coverage is close to zero, so that independently of the chosen regularization, there is no way for the inversion to recover correct velocities there.

Actually, the last three images present only very subtle differences in the continuity of some reflectors like the anticlines in the center of the image or the horizontal reflector above the reservoir. The reservoir itself seems positioned best in the two last images (Figures 13, and 14) that use the structural constraints. The similarity of the images even in the lower part contrasts with the differences of the velocity models estimated by slope tomography. This is a clear evidence of nonuniqueness in the inversion on one hand, and of the tolerance of migration to perturbation in the velocity model on the other hand. It is in these regions of nonuniqueness where regularization has its main effect.
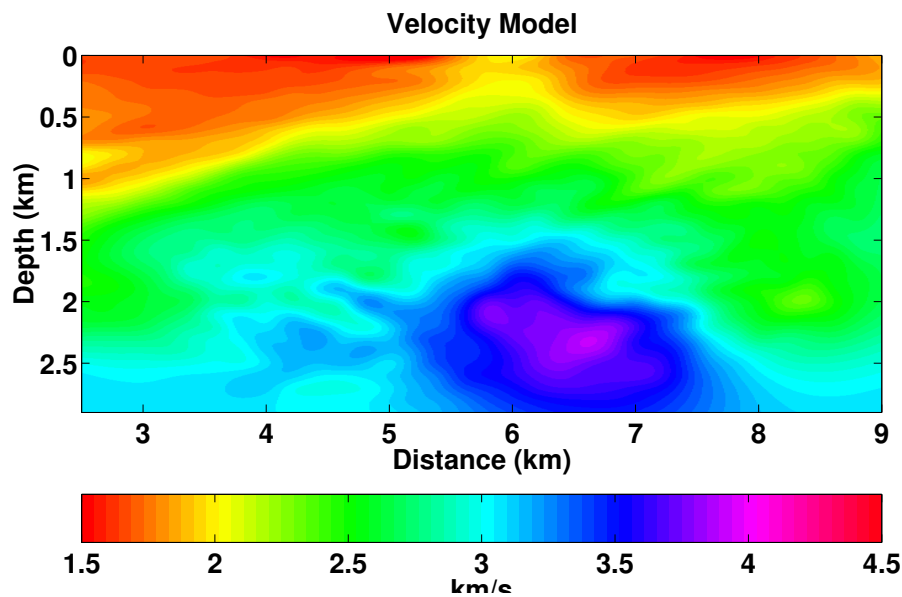
Velocity Model

Figure 4: Velocity model estimated with $\lambda_1 = 0.005$.
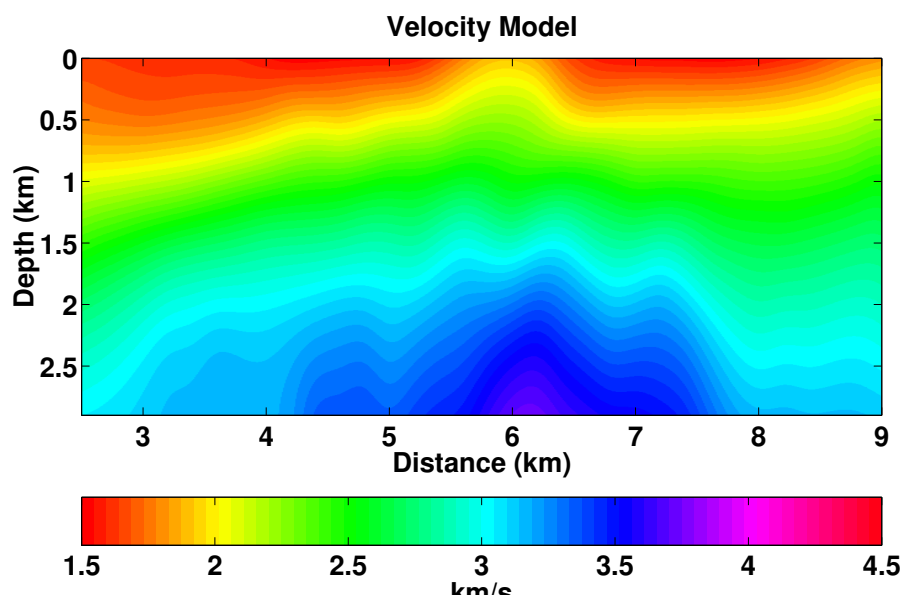
Velocity Model

Figure 5: Velocity model estimated with $\lambda_2 = 0.05$ and $\lambda_3 = 0.010$.

Angle gathers

For a more detailed analysis of the migration results, let us also compare the angle-domain common-image gathers (ADCIGs) at selected positions of the model. For each (smoothed and estimated) velocity model, we selected the ADCIGs at coordinates $x = 4.0$ km, $x = 5.0$ km, $x = 6.0$ km, $x = 6.5$ km, $x = 7.0$ km, and $x = 7.5$ km for display. Figures 15 through 20 show these results. In all these figures, panel (a) is the ADCIG calculated with the smoothed velocity model, (b) using the Laplacian constraint, (c) the curvature constraint, (d) horizontal and vertical gradient constraint, (e) the proposed structurally motivated gradient constraint, and (f) the structural plus horizontal gradient constraint. Note that due to the simulated sailing direction from left to right, only negative opening angles are illuminated.

As with the migrated images, also the ADCIGs are rather similar. Particularly in the upper part, all ADCIGs are almost identical and nicely flat, confirming again the high quality of slope tomography in
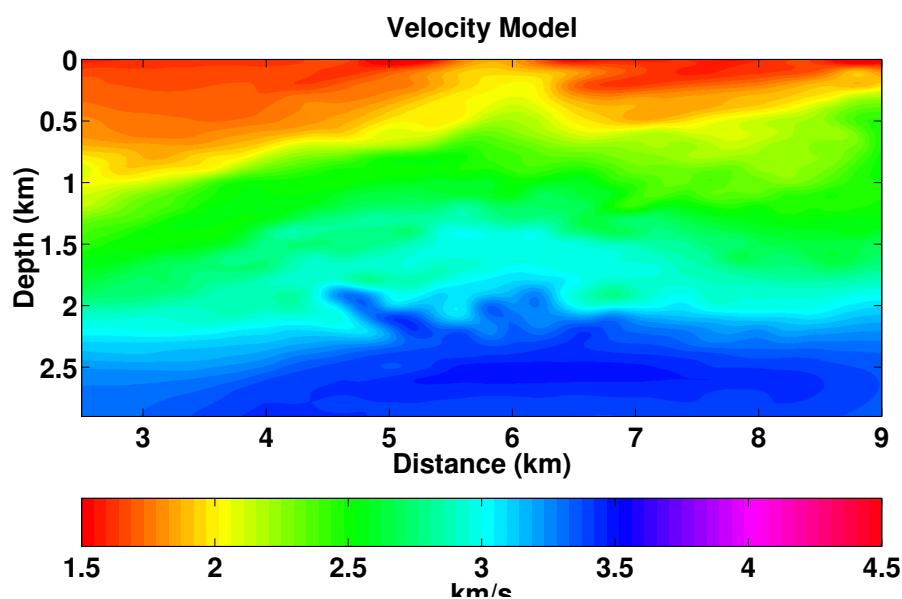
Figure 6: Velocity model estimated with $\lambda_4 = 0.050$ and $\lambda_5 = 0.010$.

areas with high ray coverage. However, there are some differences visible in the ADCIGs.

All reflectors are reasonably flat in all ADCIGs of Figure 15. Some nonflatness can only be seen in the deepest reflectors of panel (b). The main differences are in the depth position of the deeper reflectors. The best positioning is achieved in panels (e) and (f).

The differences in Figure 16 are slightly stronger. In panels (b) and (d), we see already some continuity problems with the shallow reflector at 0.4 km depth. Again, panels (e) and (f) are closest to panel (a), with panel (c) achieving good quality down to about 2.0 km.

The panels in Figure 17 are quite similar to each other down to 1.5 km. Again, panels (b) and (d) present the strongest nonflatness. At this image point, the ADCIGS (e) and (f) actually seem to provide a better image of the deeper reflectors than the smoothed model in panel (a).

Again, the upper parts of the panels in Figure 18 are very similar. The most significant differences in Figure 18 concern the reflectors below 2.0 km depth, which are reasonably flat only in panels (e) and (f).

In Figure 19, differences occur already at depths below 1.0 km. At this image point, panel (c) is not much better than panels (b) and (d). Panel (f) shows the best image of all reflectors below 1.4 km.

Finally, in Figure 20, the mispositioning in depth is the strongest. This image point is already located in the region where the tomographic inversion had the most problems because of the rather low ray coverage. Non of the recovered models places the reflectors below 1.2 km at their correct depth. Again, flatness is best in panels (e) and (f).

Evaluation

The detailed analysis of these and other ADCIGs in the model confirms our experiences from other numerical experiments with different values for the λ_i in equation (10). In the vast majority of test, a regularization with a simple Laplacian constraint leads already to reasonable models where the ray coverage is high. However, any of the other tested regularization provides better results in regions with low ray coverage. Independently minimizing both second derivatives was consistently better than minimizing the Laplacian. Minimization of the horizontal and vertical velocity gradient is generally better than the Laplacian constraint but worse than independent curvature minimization. The best results in our numerical examples were consistently achieved using the structurally motivated minimization of the gradient component in the direction of a potentially present reflector. In many cases, it is helpful to simultaneously minimize also the horizontal component.
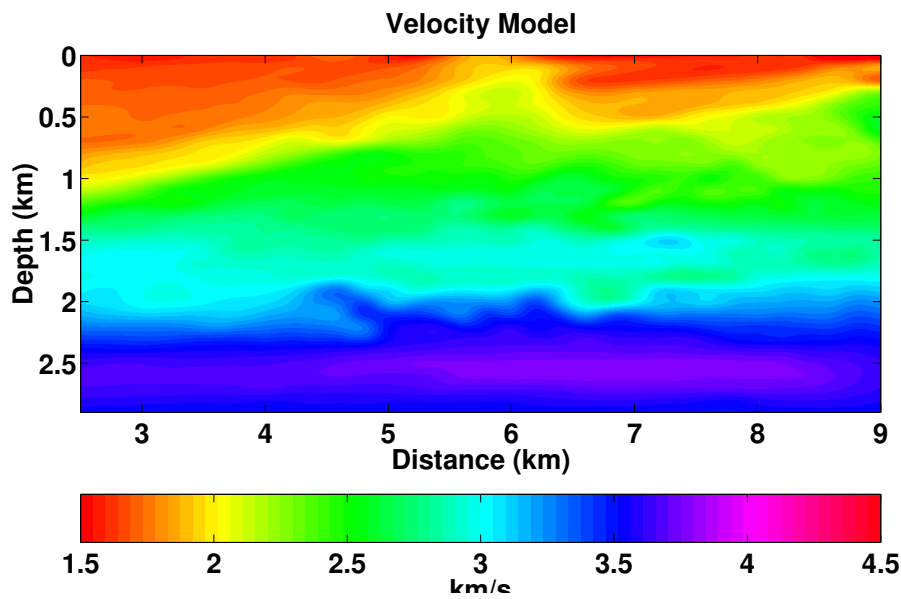
Velocity Model

Figure 7: Velocity model estimated with $\lambda_6 = 0.050$.
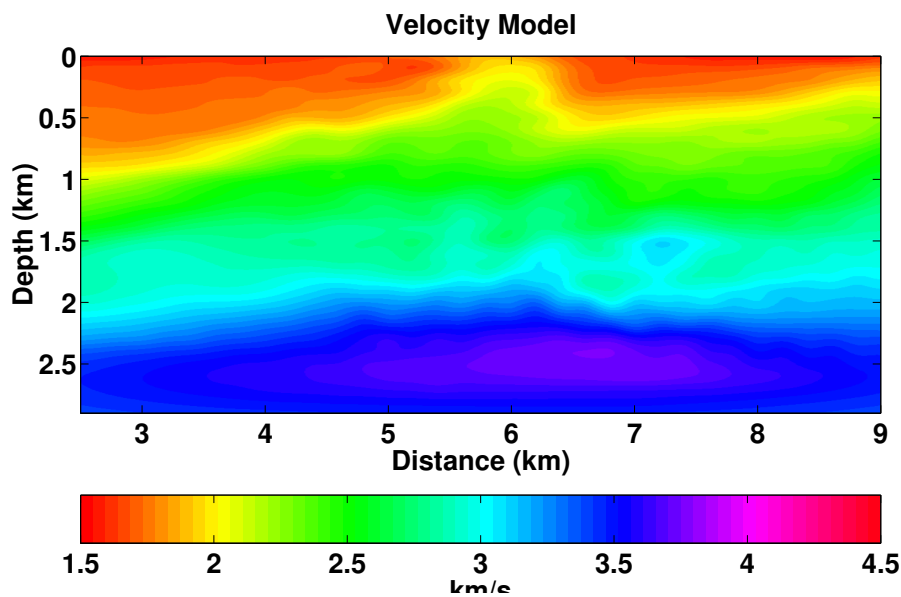
Velocity Model

Figure 8: Velocity model estimated with $\lambda_4 = 0.005$ and $\lambda_6 = 0.0025$.

CONCLUSIONS

In this paper, we have proposed a new smoothness constraint for slope tomography that minimizes the velocity gradient in the dip direction of a possibly present reflector at an image point. This potential dip direction can be estimated as the normal to the half-angle direction between the ray branches that connect sources and receivers to the image point.

To evaluate the quality of the proposed constraint, we have implemented and tested a set of different types of smoothness constraints in slope tomography. The effect of these constraints on the estimated velocity model and the corresponding seismic image was investigated with the help of numerical examples using the Marmousoft data set.

We found a clear effect of the smoothness constraints in the estimated velocity model and a less distinctive effect on the seismic imaging and ADCIGs. In our numerical tests, pure curvature constraints produced
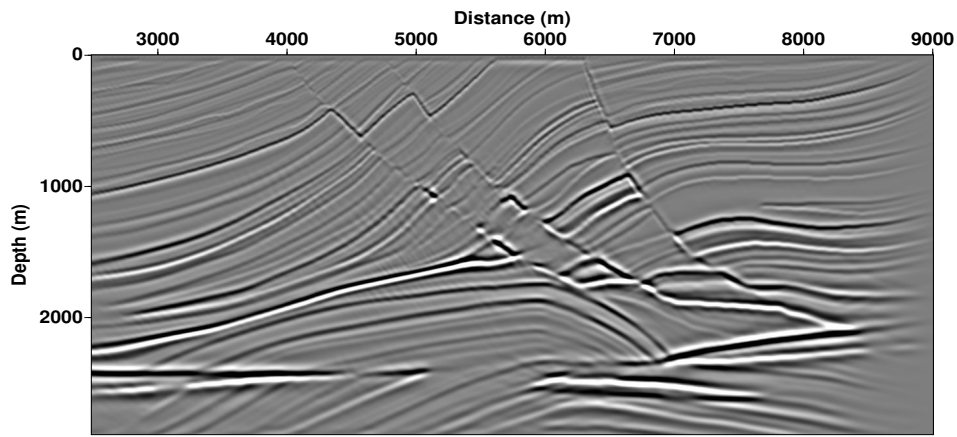
Figure 9: Post-migration stack for the smoothed velocity model in Figure 3.
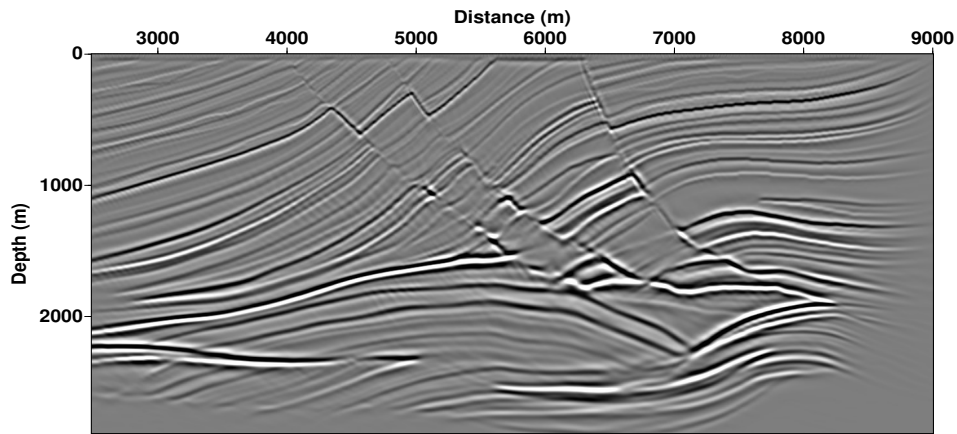
Figure 10: Post-migration stack for the estimated velocity model in Figure 4.
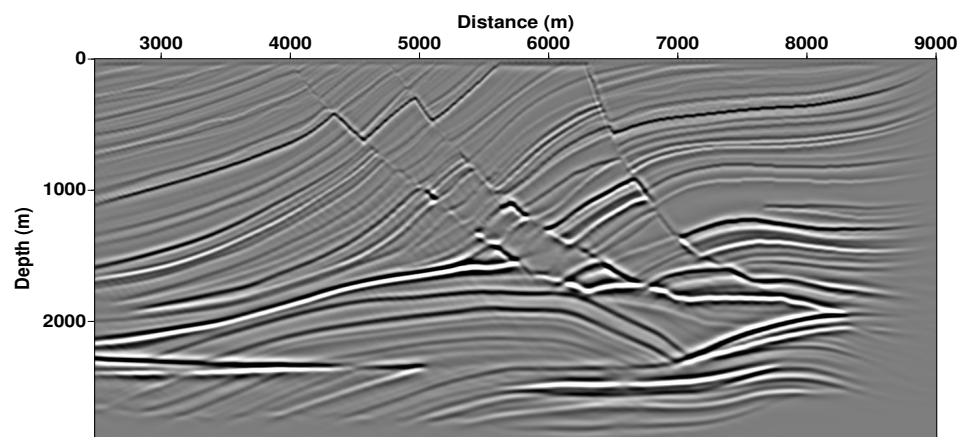
Figure 11: Post-migration stack for the estimated velocity model in Figure 5.
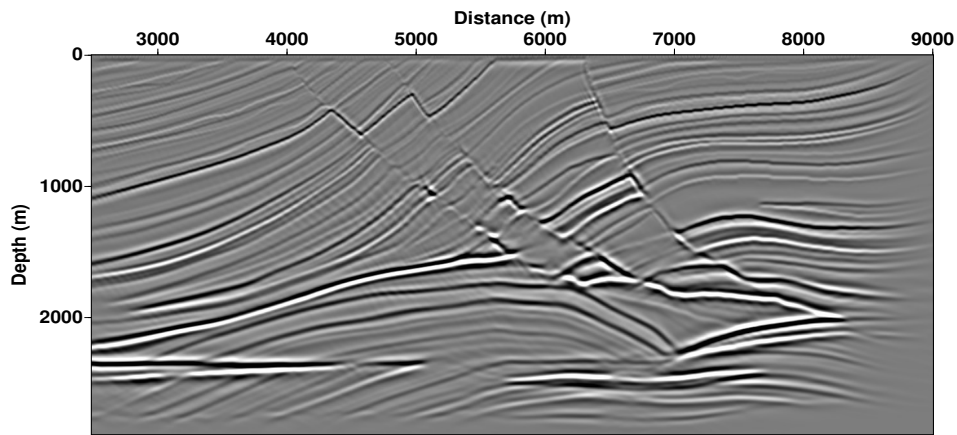
Figure 12: Post-migration stack for the estimated velocity model in Figure 6.
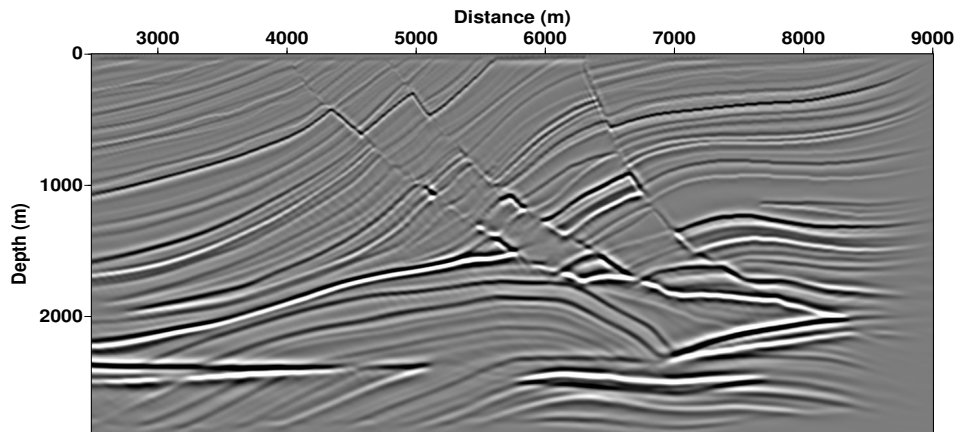
Figure 13: Post-migration stack for the estimated velocity model in Figure 7.
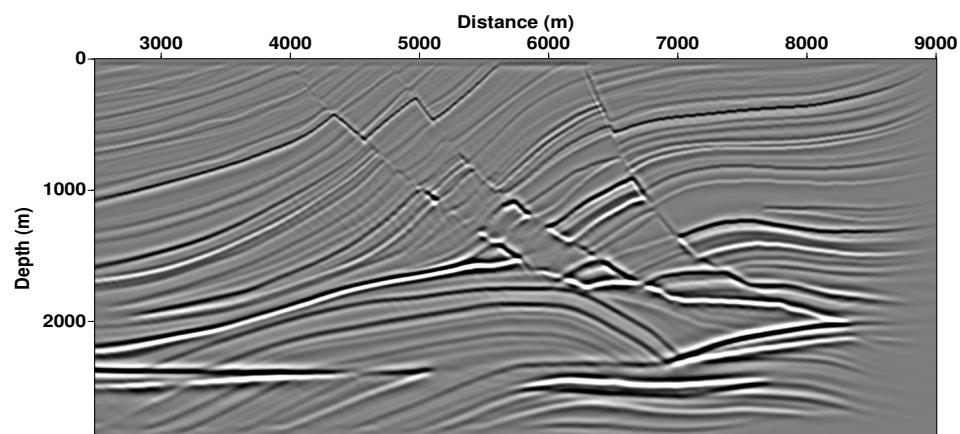
Figure 14: Post-migration stack for the estimated velocity model in Figure 8.
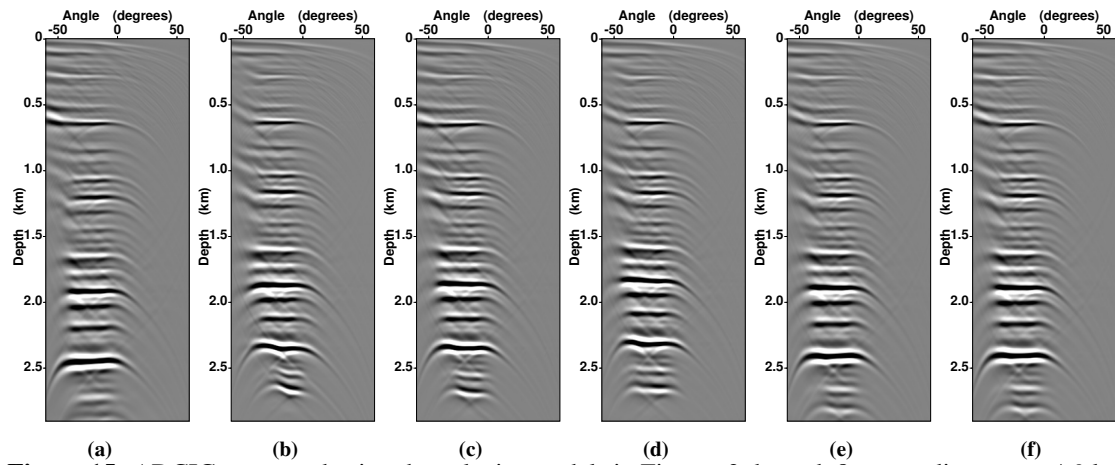
Figure 15: ADCIG computed using the velocity models in Figures 3 through 8 at coordinate $x = 4.0$ km.
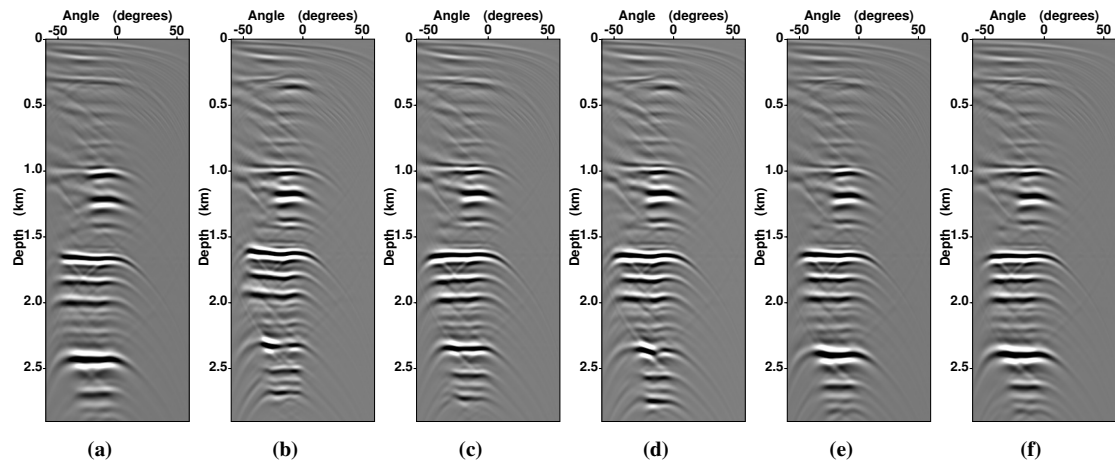
Figure 16: ADCIG computed using the velocity models in Figures 3 through 8 at coordinate $x = 5.0$ km.
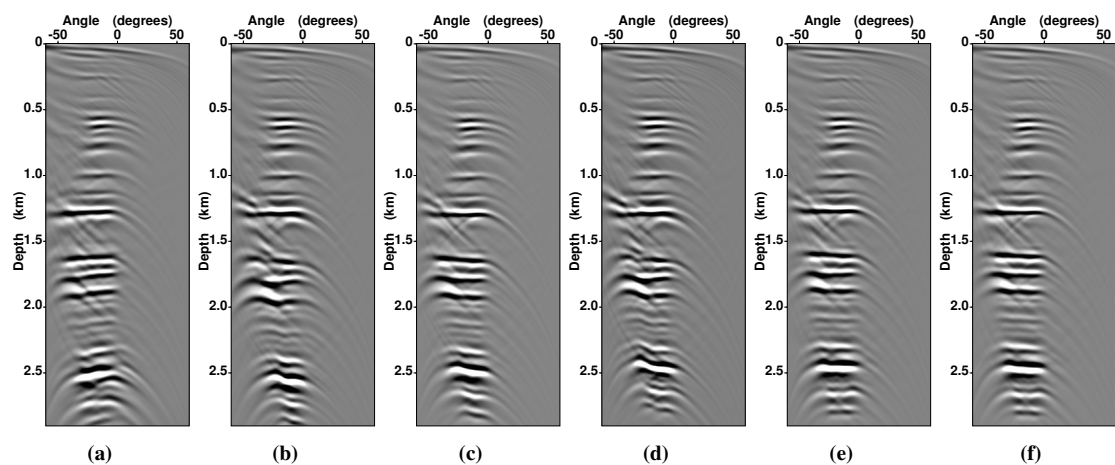
Figure 17: ADCIG computed using the velocity models in Figures 3 through 8 at coordinate $x = 6.0$ km.
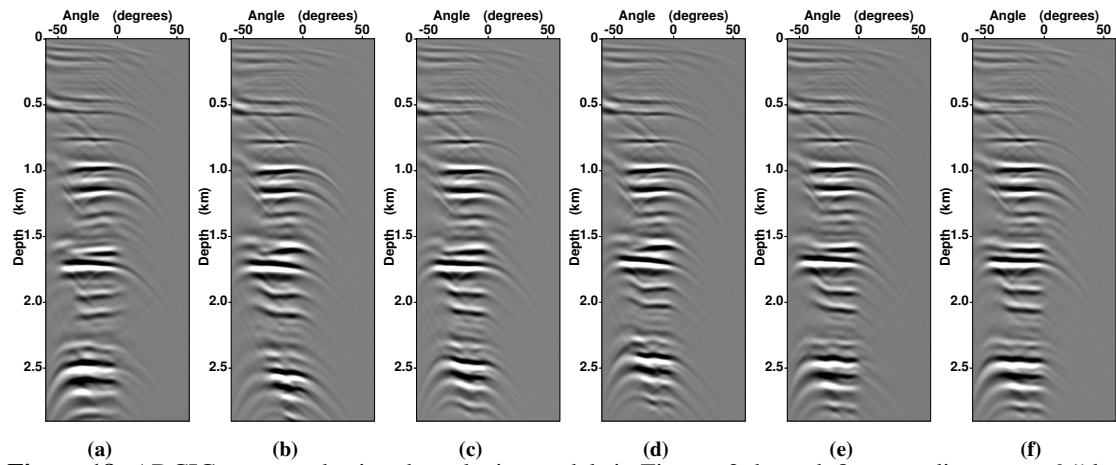
Figure 18: ADCIG computed using the velocity models in Figures 3 through 8 at coordinate $x = 6.5$ km.
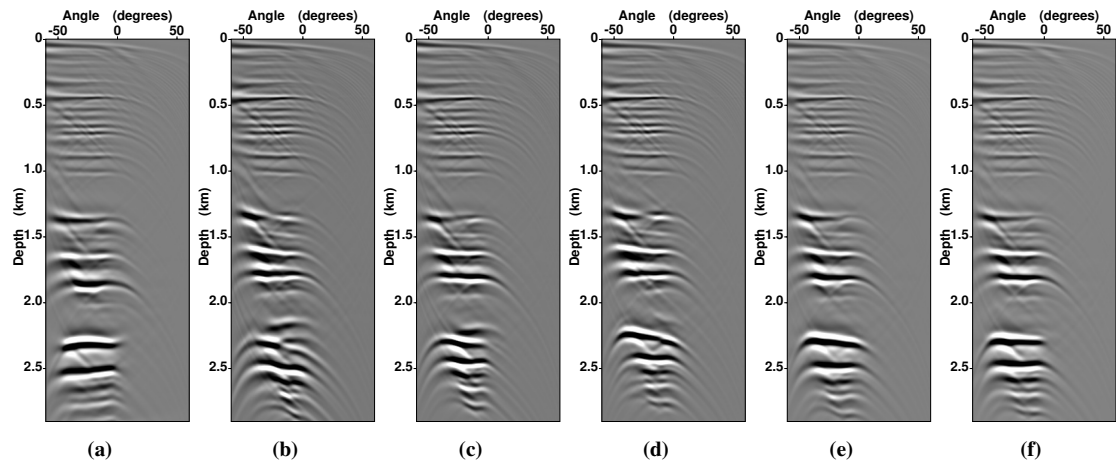
Figure 19: ADCIG computed using the velocity models in Figures 3 through 8 at coordinate $x = 7.0$ km.
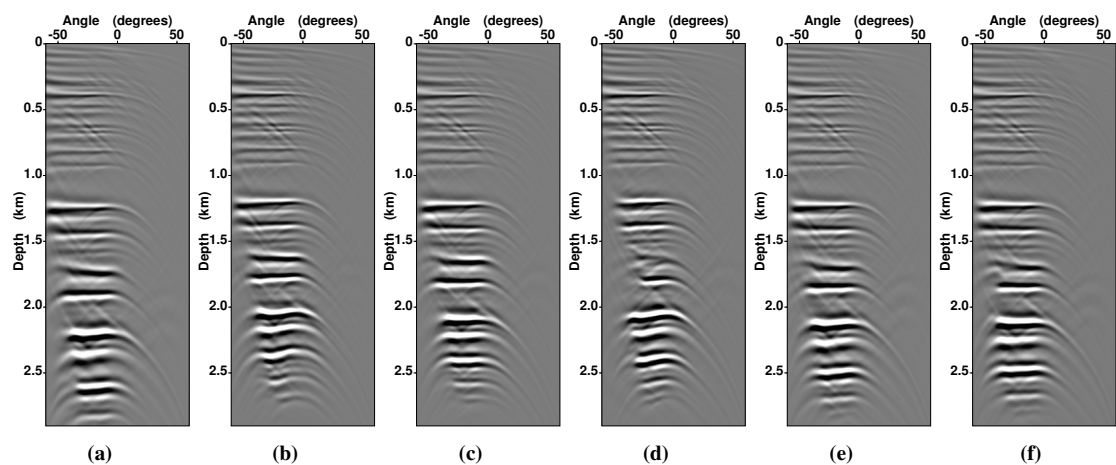
Figure 20: ADCIG computed using the velocity models in Figures 3 through 8 at coordinate $x = 7.5$ km.

worse velocity models than gradient constraints. The proposed gradient constraint in the reflector-dip direction showed a desirable behaviour. On its own or in combination with other gradient constraints, it helped to improve the obtained velocity model in areas of reduced ray coverage.

Our numerical results also indicate that the final depth-migrated images using these models may be less sensitive to the smoothness constraints than the models themselves. Not all the differences in the models actually led to differences in the final depth-migrated images. The reason is that the lower the coverage with reflection events, the stronger is the dependence of the quality of the inverted velocity model on the chosen type of smoothness constraints used to stabilize the slope tomography. Therefore, the most visible model differences will generally occur where few or no events need to be imaged. Moreover, since ray coverage generally decreases with depth, the influence of regularization increases with depth. Therefore, the final depth-migrated images will be more prone to show differences due to different regularizations at greater depth.

REFERENCES

Amazonas, D., Costa, J., Schleicher, J., and Pestana, R. (2007). Wide angle FD and FFD migration using complex Padé approximations. *Geophysics*, 72(6):S215–S220.

Billette, F. and Lambaré, G. (1998). Velocity macro-model estimation from seismic reflection data by stereotomography. *Geophys. J. Int.*, 135(2):671–690.

Billette, F., Le Bégat, S., Podvin, P., and Lambaré, G. (2003). Practical aspects and applications of 2D stereotomography. *Geophysics*, 68(3):1008–1021.

Biondi, B. L. (2006). *3-D Seismic Imaging*. Society of Exploration Geophysicists.

Bishop, T. N., Bube, K. P., Cutler, R. T., Langan, R. T., Love, P. L., Resnick, J. R., Shuey, R. T., Spindler, D. A., and Wyld, H. W. (1985). Tomographic determination of velocity and depth in laterally varying media. *Geophysics*, 50:903–923.

Clapp, R. G., Biondi, B., and Claerbout, J. F. (2004). Incorporating geologic information into reflection tomography. *Geophysics*, 69(2):533–546.

Farra, V. and Madariaga, R. (1988). Non-linear reflection tomography. *Geophysical Journal*, 95:135–147.

Menke, W. (1989). *Geophysical Data Analysis: Discrete Inverse Theory*, volume 45 of *International Geophysics*. Academic Press, 2nd edition.

Rickett, J. and Sava, P. (2002). Offset and angle-domain common image-point gathers for shot-profile migration. *Geophysics*, 67(3):883–889.

Sava, P. C. and Fomel, S. (2003). Angle-domain common-image gathers by wavefield continuation methods. *Geophysics*, 68(3):1065=961074.

Sinoquet, D. (1993). Modeling a priori information on the velocity field in reflection tomography. In *63rd Annual International Meeting, SEG, Expanded Abstracts*, pages 591–594.

Tessmer, E. (2003). Full-wave pre-stack reverse-time migration by the Fourier method and comparisons with Kirchhoff depth migration. *Annual WIT Report*, 7:163–176.